Capturing the interconnectivity of water-induced oxidation and sintering of cobalt nanoparticles during the Fischer-Tropsch synthesis *in situ*

Moritz Wolf,[†,1] Nico Fischer,[†] and Michael Claeys*[,†]

[†]Catalysis Institute and DST-NRF Centre of Excellence in Catalysis c*change, Department of Chemical Engineering, University of Cape Town, Rondebosch 7701, South Africa.
*Corresponding author: Email michael.claeys@uct.ac.za

Abstract

Supported nano-sized metal crystallites as catalysts in the Fischer-Tropsch synthesis have become a major research focus due to their high mass specific surface area and resulting lower cost. Such small supported cobalt crystallites have been reported to show a very different resistance with regard to deactivation compared to larger cobalt particles. The Fischer-Tropsch product water is reported to have a severe effect on the deactivation of cobalt-based Fischer-Tropsch catalysts. Compared to other water-induced deactivation mechanisms, hydrothermal sintering of cobalt nanoparticles is fairly well established in literature. A previously hypothesised interconnection between oxidation of cobalt nanoparticles and hydrothermal sintering has – for the first time – been captured *in situ* in the presented study. High concentrations of water induce oxidation of the cobalt nanoparticles increasing their mobility and resulting in crystallite growth *via* particle migration and coalescence whilst in the oxidised state. A well-defined model catalyst comprising highly dispersed cobalt nanoparticles on a relatively inert exfoliated graphite support in combination with an *in situ* magnetometer allowed for these observations, which resulted in irreversible deactivation of the catalyst.

Keywords

Fischer-Tropsch synthesis; oxidation; sintering; deactivation; magnetometer; cobalt catalyst; model catalyst; water.

1. Introduction

Water is a major product of the Fischer-Tropsch synthesis (FTS) and generally accepted to induce deactivation of nano-sized supported cobalt catalysts [1–6]. However, the actual occurrence and contribution of water-induced deactivation processes are highly controversially discussed in literature [1–5,7–9]. The discrepancy can mostly be ascribed to inadequate model systems, as well as the application of characterisation techniques that cannot monitor the metallic cobalt phase directly and at relevant conditions [2]. While the detrimental effect of water on the stability as a result of sintering is fairly well established in the literature [7,8,10], views on water-induced oxidation are very divided [1–4]. However, several studies attempting to clarify deactivation by oxidation of the Fischer-Tropsch (FT) active cobalt phase by H_2O have been published recently providing a more unified view [6,11–13]. An interconnection between both, oxidation of cobalt nanoparticles to cobalt oxide and hydrothermal sintering, has been hypothesised [8]. In the Co-based FTS, the surface oxidation/reduction cycle of CO cleavage and H_2O formation is hypothesised to be accompanied by a continuous structural re-arrangement leading to a higher mobility of the cobalt atoms and resulting in crystallite growth [14]. Hydrothermal sintering results in a loss of active surface area due to an increase of the average crystallite diameters [15]. The correlation between the presence of H_2O and Co crystallite growth during FTS has been reported in several studies [7,8,14,16–19] and was recently summarised by Claeys *et al.* [10].

In the present study, a recently developed model catalyst comprising of highly dispersed cobalt nanoparticles with well-defined sizes on a rather inert graphitic support [20] was exposed to H_2O-rich atmospheres mimicking high conversion FT environments. The stability of the supported cobalt nanoparticles in H_2O/H_2 atmospheres was monitored *in situ* in an in-house developed magnetometer [21]. The utilisation of carbon as support material minimises the feasibility of a chemical reaction between the metal and the support [7,13], *e.g.* the formation of metal support compounds [6,22–24]. In fact, the applied pristine exfoliated graphite (EG) only provides limited stabilisation due to weak metal-support interactions [20]. The partial pressure of CO (0.69 bar) was sufficiently high in order to induce a potential thermodynamically controlled, H_2O-driven indirect oxidation of Co nanoparticles to CoO by H_2O [13].

2. Materials and methods

2.1 Chemicals

Acetone (CH_3COCH_3; ≥99.3%), ammonia solution ($NH_4OH_{(aq)}$; 25 wt.%), and ethanol (CH_3OH; 99.9%) were purchased from Kimix (South Africa). Benzyl alcohol (C_7H_8O; ≥99.0%), Cobalt(II) acetate tetrahydrate ($Co(CH_3CO_2)_2 \cdot 4H_2O$), and n-methyl-

2-pyrrolidone (C_5H_9NO) were purchased from Sigma-Aldrich. Kaylaw graphite powder was obtained from Electrochem (South Africa).

2.2 Synthesis of well-defined Co_3O_4 nanoparticles

Nanoparticles were synthesised *via* a surfactant-free, nonaqueous heat treatment of dissolved cobalt acetate in benzyl alcohol in the presence of ammonium hydroxide [12,13,25,26]. Cobalt(II) acetate tetrahydrate (1600 mg; impurities of cobalt(II) oxide acetate were identified; Figure S7) was dissolved in 70 mL benzyl alcohol under magnetic stirring at 500 rpm in a round bottom flask. After 2 h of stirring, 70 mL of 25 wt.% aqueous ammonium hydroxide solution was added dropwise to the solution forming an emulsion. Once the addition of ammonium hydroxide was completed, the flask including the stirrer bar was immediately transferred to a preheated oil bath of a rotary evaporator (165 °C) and heated for 3 h at a set pressure of 900 mbar and rotation at 180 rpm. Ambient air was bubbled through the reaction emulsion throughout the synthesis to ensure ideal mixing [26]. After cool-down to room temperature, the volume was tripled with diethyl ether and the mixture was centrifuged for 1 hour at 7000 rpm. The centrifugate containing the nanoparticles was re-dispersed in ethanol and washed at least three times with acetone until a clear supernatant was obtained.

2.3 Exfoliation of graphite

Kaylaw graphite powder was exfoliated to increase the surface area [20,27]. The organic compound 1-Methyl-2-pyrrolidinone (NMP) facilitates the exfoliation as the surface energy is very close to that of graphite [28]. An amount of 3300 mg graphite powder was sonicated in 1000 mL NMP for 12 h [28]. The suspension was centrifuged at 500 rpm for 45 min to separate non-exfoliated and larger flakes of graphite [27]. The exfoliated graphite (EG) in the remaining supernatant was collected *via* centrifugation at 7000 rpm for 2 h, subsequently washed several times with acetone, and dried at 80 °C in an oven (Memmert).

2.4 Decoration of the support

A separate preparation of well-defined crystallites with subsequent deposition onto a support material allows for the synthesis of tuneable model catalysts [11–13,29–31]. The synthesised Co_3O_4 crystallites were dispersed in ethanol in an ultrasonic bath until all nanoparticles were in dispersion (approximately 10-16 h). The EG support was sonicated for 4 h in ethanol after which the dispersion of Co_3O_4 nanoparticles in ethanol was added dropwise targeting a desired loading of metallic Co of 3 or 1 wt.% in order to compare the stability of differently crowded nanoparticles during reduction in H_2. After sonicating for another 4 h, the dispersion was transferred to a rotary evaporator and further mixed for 1 h at 240 rpm and 80 °C. Subsequently, ethanol was evaporated from the parent catalyst at 462 mbar and the catalyst was dried at 80 °C.

2.5 *Ex situ* characterisation

X-ray diffraction (XRD) was conducted at 35 kV and 40 mA in a D8 Advance X-ray diffractometer (Bruker AXS), equipped with a cobalt source ($\lambda_{K\alpha1}$ = 1.78897 Å; slit width = 1.0 mm) and a LYNXEYE XE position sensitive detector (Bruker AXS) from 20-120° at a step size of 0.025° with an exposure time of 1 s per step. Obtained XRD patterns were compared to reference patterns of the Powder Diffraction File of the International Centre for Diffraction Data (ICDD; PDF-2 Release 2008, ref. [32]; Co_3O_4: 00-043-1003, $Co(C_2H_3O_2)_2 \cdot 4H_2O$: 00-001-0110, $Co_6O(C_2H_3O_2)_{10}$: 00-022-0244). Volume mean crystallite sizes with associated errors were determined by Rietveld refinement [33] of the XRD patterns (TOPAS 5, Bruker AXS, ref. [34]). The instrumental line broadening was modelled *via* fitting the pattern of corundum with additional convolutions. Diffraction line broadening analysis *via* the Scherrer equation [35] (Co_3O_4: 311 diffraction) with correction for the instrumental line broadening and a shape factor of 0.9 was applied as a second method to estimate the crystallite size [36].

Samples were analysed by means of **transmission electron microscopy (TEM)** in a Tecnai 20 microscope (FEI) equipped with a LaB_6 field emission gun and operated at 200 kV. The TEM is fitted with a Tridiem GIF with 2kx2k CCD camera (Gatan). Nanoparticles were dispersed in ethanol *via* ultrasonication for 30 min. In contrast, catalysts were mixed with acetone and dispersed in the ultrasonication bath for 1 min (parent catalysts) or 3 min (spent catalysts). The dispersion was subsequently deposited onto carbon-coated copper grids for analysis. Size distributions of cobaltous crystallites were determined by measuring the size of over 500 nanoparticles in the as prepared Co_3O_4 sample, the supported catalyst, as well as in the spent catalyst after FTS using the open-source ImageJ 1.51a software package [37]. The obtained number-based size distributions were converted to volume-based size distributions. The number mean size ($d_{n,TEM}$), the volume mean size ($d_{V,TEM}$), and the relative volume-based standard deviation ($\sigma_{V,TEM}$) were calculated according to Equations (1-3), respectively.

$$d_{n,TEM} = \frac{\sum_{i=1}^{N} d_i}{N} \tag{1}$$

$$d_{V,TEM} = \frac{\sum_{i=1}^{N} n_i \cdot d_i^4}{\sum_{i=1}^{N} n_i \cdot d_i^3} \tag{2}$$

$$\sigma_{V,TEM} = \sqrt{\frac{\sum_{i=1}^{N}\left(n_i \cdot d_i^3\left(d_i - d_{V,TEM}\right)^2\right)}{\frac{N-1}{N}\sum_{i=1}^{N} n_i \cdot d_i^3}} \Bigg/ d_{V,TEM} \cdot 100\% \tag{3}$$

Where d_i are the measured sizes, N is the number of measured particles, and n_i are the particular fractions.

The surface area of the graphitic support material was analysed *via* physisorption according to the **Brunauer-Emmett-Teller (BET) method**. The pore volume with associated error and pore size were obtained by applying the **Barrett-Joyner-Halenda**

(BJH) method [38]. Physisorption was conducted using a TriStar II 3020 (Micromeritics) with N_2 as analysis adsorptive and a degassing temperature of 200 °C.

Samples for elemental analysis *via* **inductively coupled plasma optical emission spectrometry (ICP-OES)** were pre-treated overnight in a 4:1 molar ratio of aqua regia:HF corresponding to a 3:1:1 mixture of $HCl:HNO_3:HF$. Subsequently, the mixture was heated at a rate of 6.4 °C min^{-1} to 180 °C for 40 min during microwave digestion (1600 W) in order to obtain the cobalt loadings or metal concentrations *via* elemental analysis in a Varian ICP-OES 730 (Agilent).

2.6 *In situ* magnetometry

The *in situ* magnetometer is a fixed-bed reactor enabling the exposure of a solid sample to increased pressures and temperatures at various atmospheres, which is placed between the pole caps of a strong external electromagnet (see supporting material, Figures S1-4 and references [10,11,13,21] for detailed set-up and methodology). It is the ideal characterisation technique to study phase transformations in metallic Ni-, Fe-, and Co-based catalysts as the various phases and their oxidic counterparts display unique magnetic properties. Phase specific magnetic susceptibilities, Curie or Néel temperatures, threshold sizes for superparamagnetic behaviour, etc. allow for a distinct identification and quantitative characterisation of particular phases. For example, the magnetic characterisation of Co model catalysts provides highly accurate information on the amount of metallic Co, *i.e.* only phase transformations involving the metallic phase are monitored as all oxidic cobalt species are anti-ferromagnetic with Néel temperatures below room temperatures [39] and ferromagnetic cobalt carbides display very low magnetic susceptibilities [40]. Hence, the magnetisation of the model catalysts in the strong external magnetic field of the magnetometer up to 2 T correlates to the amount of metallic, ferromagnetic Co present in the fixed-bed reactor. Oxidation of Co results in a decrease of the magnetisation, whilst reduction of oxidic Co phases to metallic Co results in an increase. The saturation magnetisation (M_S) of the sample is approximated in a 6-point measurement (Figure S4) *via* averaging the measured magnetisations at the maximal external field strength of +2.0 and -2.0 T. This magnetisation can be compared to the magnetisation of a calibration sample of 100 mg metallic bulk cobalt at various temperatures ($M_{S,cal}$; Figure S6) to obtain the degree of reduction (DOR; Equation 4).

$$DOR = \frac{M_S(T)}{M_{S,cal}(T)} \cdot \frac{100 \text{ mg}}{m_{cat} \cdot x_{Co}} \cdot 100\% \qquad (4)$$

Where m_{cat} is the mass of loaded catalyst and x_{Co} is the Co loading of the catalyst.

In addition, measurement of the remnant magnetisation upon removal of the external field (M_{rem}) allows for conclusions to be made on the crystallite size [39]. Small fcc-Co crystallites below 15 nm are not capable of retaining a remnant magnetisation

upon removal of an external magnetic field as they display superparamagnetism [39,41]. It has to be noted, that this threshold size is still under debate and may be even smaller [7,13,42]. The fraction of Co retaining magnetisation (γ) describes the percentage of crystallites larger than this threshold size (Equation 5). In addition, the measurement of the sample's magnetisation as a function of the external field strength can be described by the Langevin equation for superparamagnetic nanoparticles (Equation 6), which can be fitted with a set of phase specific and size-dependent equations (Figure S5) in order to obtain a size distribution of the superparamagnetic phase [39]. Furthermore, extrapolation of the magnetisation at high external field strengths to the inverse external field strengths provides a second, more accurate way to obtain the saturation magnetisation of the samples. In the case of a hysteresis behaviour of the sample's magnetisation as a function of the external field strength ($\gamma > 0$ wt.%), the anhysteretic contribution to the hysteresis can be modelled according to the Jiles-Atherton method [43–46] (see supporting material, Equations S1-5; ref. [13] for validation) before applying the Langevin equations. The obtained size distribution then describes the superparamagnetic fraction of Co crystallites exclusively.

$$\gamma(T) = \frac{2 \cdot M_{rem}(T)}{M_S(T)} \cdot 100 \text{ wt.\%} \qquad (5)$$

$$\frac{M(T)}{M_S(T)} = \coth\left(\frac{\rho \cdot \sigma_S \cdot \pi \cdot d^3 \cdot H}{6 \cdot k \cdot T}\right) - \frac{6 \cdot k \cdot T}{\rho \cdot \sigma_S \cdot \pi \cdot d^3 \cdot H} \qquad (6)$$

Where ρ is the density of the magnetic material, d is the diameter of the magnetic crystallites, k is the Boltzmann constant, and σ_S is the mass specific saturation magnetisation of the magnetic material at standard temperature.

In the present study, a total amount of 505.4 mg of the 3 wt.% or 752.7 mg of the 1 wt.% oxidic parent Co_3O_4/C catalyst were placed in the reactor. The samples were then reduced in a 50% H_2 in Ar atmosphere at a gas hourly space velocity (GHSV) of 6000 mL ($g_{catalyst}$ h)$^{-1}$. The high GHSV was intended to prevent strong concentration gradients of formed water over the catalyst bed during the reduction, which may inhibit the reduction [47] or even induce sintering of the well-defined supported cobaltous nanoparticles. The reduction temperature was 300 °C with a heating rate of 1 °C min^{-1} and a holding time of 5.5 and 18 h for the 3 wt.% and 1 wt.% catalyst, respectively. After reduction, the 1 wt.% catalyst was exposed to dry synthesis gas in N_2 with a H_2/CO ratio of 2.11 at a high GHSV of 17537 mL ($g_{catalyst}$ h)$^{-1}$ to keep the actual FT conversion low, *i.e.* to minimise the partial pressure of H_2O at the reactor outlet. Afterwards, H_2O was co-fed *via* an HPLC-pump and a vaporiser increasing the partial pressure of H_2O incrementally to simulate various FT conversion levels. The amount of co-fed H_2O and the absolute pressure were adjusted accordingly to obtain p_{H2O}/p_{H2} ratios of 0.5-5 (Table 1). The p_{H2O}/p_{H2} ratio describes the ratio of the FT product H_2O over the FT reactant H_2

6

and is highly relevant for the stability of Co nanoparticles against oxidation by H_2O [2,48]. All H_2O levels were monitored for at least two hours before changing to the next condition. The reversibility of potential oxidation under dry synthesis gas was tested in a last step by removing the co-fed H_2O, *i.e.* at the initial conditions. After cool-down to room temperature, the catalyst was passivated in 1% O_2 at a GHSV of 1500 mL ($g_{catalyst}$ h)$^{-1}$ for several hours [49] and recovered for additional *ex situ* characterisation.

Table 1 Applied conditions for the incremental increase of the simulated Fischer-Tropsch conversion levels *via* co-feeding water during *in situ* magnetic measurements after catalyst reduction.

H_2O level	p_{H2} / bar	p_{CO} / bar	p_{Ar} / bar	p_{H2O} / bar	p_{H2O}/p_{H2}	$X_{CO,sim}$ / %	$d_{crit,fcc-Co}$ / nm [48]	p / bar
-	1.45	0.69	0.46	-	0.00	-	-	2.60
1	1.45	0.69	0.46	0.73	0.50	53.85	3.44	3.33
2	1.45	0.69	0.46	1.45	1.00	70.00	3.77	4.05
3	1.45	0.69	0.46	3.63	2.50	85.37	4.38	6.23
4	1.45	0.69	0.46	7.26	5.00	92.11	5.04	9.86
-	1.45	0.69	0.46	-	0.00	-	-	2.60

Product gas was sampled *via* the ampoule method [50] and analysed in an off-line Varian CP 3900 gas chromatograph (Agilent) equipped with a flame ionisation detector (FID). A CP-Sil 5CB (Agilent) capillary column (length: 25 m, inner diameter: 0.15 mm, film thickness: 2 μm) was used at a column pressure of 1.72 bar. The product gas was injected into the GC-FID via a syringe and a split ratio of 20 was used at an injection temperature of 200 °C. The oven temperature was kept at -55 °C for 1.5 min through cooling with liquid CO_2, subsequently heated to 0 °C at a heating rate of 20 °C min^{-1}, further heated to 100 °C at 14 °C min^{-1}, and finally heated to 280 °C at 16 °C min^{-1} resulting in a total analysis time of 25 min. The detector was operated at 200 °C. A makeup gas flow of 15 mL min^{-1} N_2, a flame gas flow of 30 mL min-1, and an air flow of 200 mL min^{-1} were pre-set. Cyclohexane (0.17 vol.% in N_2) was co-fed as an internal standard and partially replaced Ar in the corresponding parts of the experiment. The low CO conversions in the present study were calculated from the formation rates of C_1-C_6 hydrocarbons using the internal standard. The certainty of resulting selectivities and conversions is calculated by the variance of the analyses of at least three samples.

3. Results and discussion

The herein utilised EG support has recently been thoroughly characterised by means of XRD, Raman, BET analysis, TEM, and thermogravimetric analysis (TGA) [20]. As expected for pristine graphitic carbon, a low degree of functionalisation of the surface was identified. Further, exfoliation of the parent graphite powder in combination with

a size selection process increases the BET surface area from 25.8 ± 0.1 to 47.8 ± 0.2 m^{2}g^{-1} [20]. Expectedly, the pore volume of 0.164 cm^{3}g^{-1} is negligibly small (Figure S8). The separately synthesised Co_3O_4 nanoparticles were characterised by means of XRD and TEM. The absence of any other phase than Co_3O_4 (Figure 1) confirms the reported high purity of the material prepared *via* the applied synthesis procedure [25,26]. Rietveld refinement results in a volume-mean crystallite size of 4.9 nm, which is confirmed by the application of the Scherrer equation (5.0 nm) and analysis of TEM images (4.6 nm; Figure 2a). TEM analysis also reveals the uniformity of the nanoparticles with a small volume-based relative standard deviation of 16.2% and a cubic morphology. Supporting these separately synthesised nanoparticles onto the prepared EG *via* ultrasonication [12,13,20,29] yields well-dispersed, rather isolated nanoparticles (Figure 2b-c). Elemental analysis of the resulting 3 and 1 wt.% Co/EG model catalysts by means of ICP-OES results in actual loadings of 2.82 and 0.95 wt.%, respectively. The reduction behaviour of similar model catalysts has been previously characterised in an *in situ* XRD study [20]. In order to maintain the well-defined characteristics of the nanoparticles during reduction to metallic fcc-Co, the loading had to be reduced from 5 to 1 wt.% Co to achieve an absence of significant sintering.
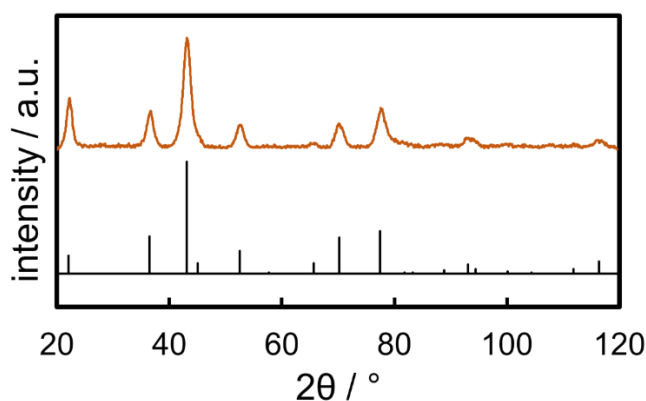

Figure 1   X-ray diffraction pattern of the synthesised Co_3O_4 nanoparticles with a reference pattern for Co_3O_4.
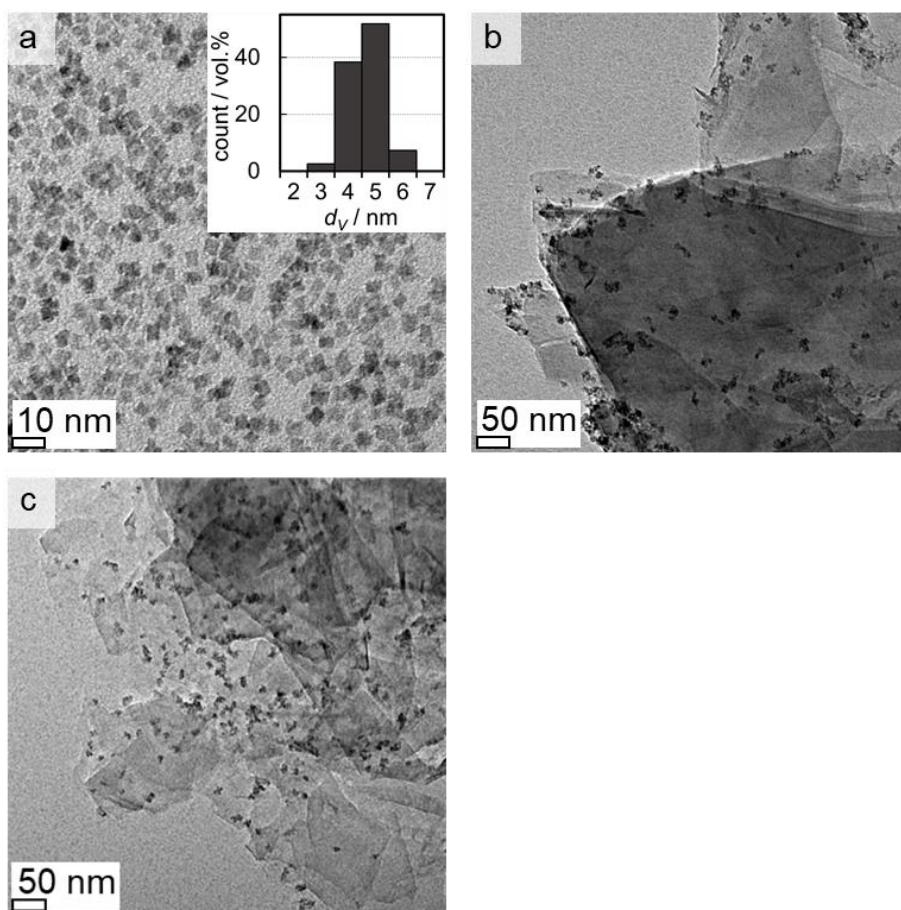
Figure 2   Transmission electron micrographs of (a) the synthesised Co_3O_4 nanoparticles with volume-based size distribution, as well as micrographs of the prepared parent Co_3O_4/C catalysts with (b) 3 wt.% and (c) 1 wt.% loading of cobalt.

The reduction of the supported Co_3O_4 nanoparticles in the two model catalysts in H_2 was monitored in an *in situ* magnetometer, which is highly sensitive towards the presence/formation of metallic ferromagnetic Co, while oxidic cobalt species cannot be detected at given temperatures. The reduction to metallic Co starts at comparable temperatures of 255 °C and 260 °C for the 1 and 3 wt.% Co loaded samples, respectively (Figure 3a). The γ value, describing the fraction of Co crystallites larger than the threshold size for superparamagnetism and hence indicating changes in crystallite size, decreases during the reduction at 300 °C (Figure 3b), presumably due to the ongoing reduction (Figure 3a) of rather isolated nanoparticles forming small superparamagnetic metallic nanoparticles and hence reducing the overall γ value (Figure 3b). This reduction behaviour is in strong contrast to the catalyst with a 1 wt.% Co loading, which reduces almost exclusively to superparamagnetic Co crystallites, even during the initial temperature ramp (Figure 3b). A continuous decrease of the γ value is identified during the 18 h holding time at 300 °C. Consequentially, a low loading of 1 wt.% Co is required in order to limit significant size increases. As in our previous study employing EG as a support for 5 and 1 wt.% Co/C model catalysts [20], the lower loading prevents major

9

agglomerates in the parent model catalyst and allows for the conservation of the well-defined sizes of most nanoparticles.
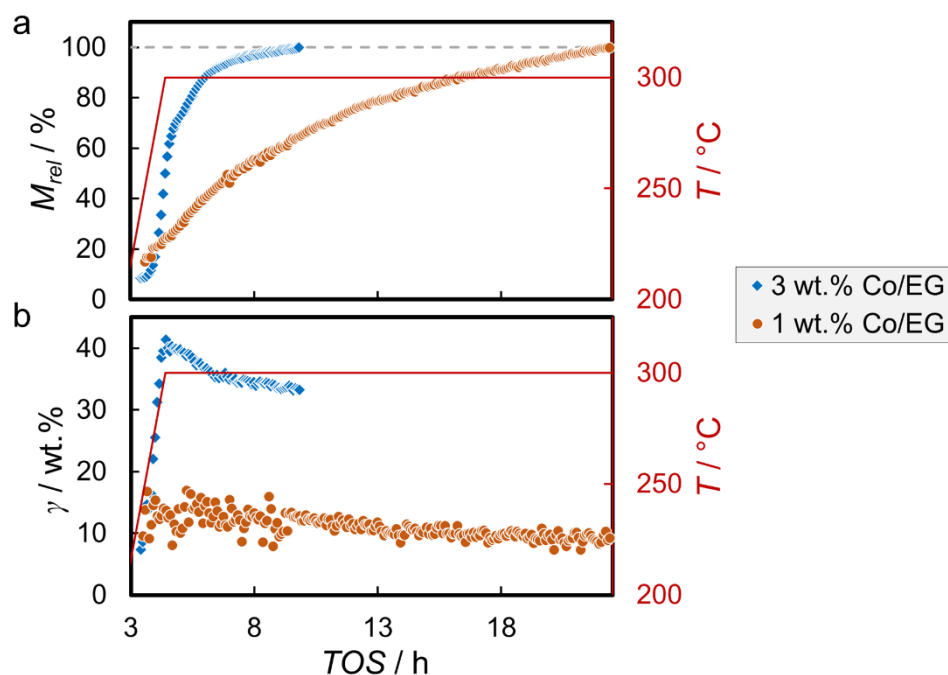

Figure 3   (a) Magnetisation at maximum external field strength (2 T) relative to the magnetisation after reduction and (b) fraction of cobalt displaying remnant magnetisation as a function of time on stream and temperature during reduction of 3 and 1 wt.% Co on exfoliated graphite in hydrogen at 300 °C (1 °C min^{-1}) for 6 h and 18 h, respectively.

The slopes of the reduction curves, either as function of the temperature during the initial ramp or as function of the holding time at 300 °C, provide valuable characteristics of the reduction behaviour of a catalyst. They can easily be described by the first derivative of the magnetisation as function of the temperature or the holding time, respectively. The former features one maximum for both model catalysts (Figure 4a). Such an accelerated rate of reduction may indicate the simultaneous reduction of nanoparticles in close vicinity *via* H* spillover, an autocatalytic reduction [51–53], which can be expected for the reduction of agglomerates or even completely unsupported nanoparticles [20]. The 3 wt.% Co/EG catalyst features a pronounced maximum before the holding time at 300 °C corresponding to a simultaneous reduction of a rather large amount of oxidic cobalt to the metallic phase, potentially *via* the aforementioned H* spillover mechanism. Contrarily, the slow reduction of nanoparticles in the 1 wt.% Co/EG catalyst results in a less intense, rather wide maximum (Figure 4a). This characteristic feature suggests a high dispersion of the nanoparticles over the support resulting in a pronounced stabilisation by the support.
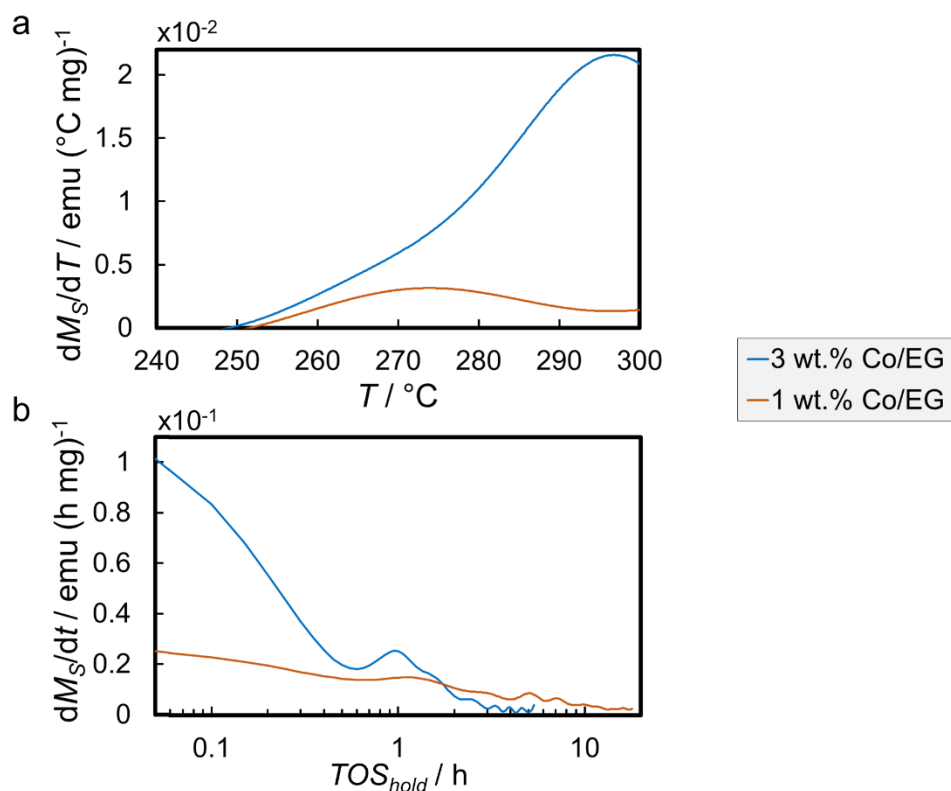
Figure 4 First derivative of the magnetisation at maximal field strength (2 T) as a function of (a) the temperature during the initial ramp (1 °C min^{-1}) and (b) the holding time during reduction of 3 and 1 wt.% Co on exfoliated graphite in hydrogen at 300 °C for 6 or 18 h, respectively.

The derivative as a function of the holding time of the 1 wt.% loaded catalyst decreases almost continuously and follows an exponential decay demonstrating the steady reduction of rather isolated nanoparticles at 300 °C (Figure 4b). In contrast, the slope of the magnetisation of the 3 wt.% loaded catalyst drops when reaching the holding temperature, peaks again after the first hour at 300 °C, and eventually drops to negligibly small values (Figure 4b). These three sections of the reduction are indicative of the inhomogeneous dispersion of the nanoparticles over the support due to crowding of the support surface, which leads to easy-to-reduce agglomerates aside from harder-to-reduce isolated nanoparticles. The 1 wt.% Co/EG catalyst mostly features the latter class.

Measuring the magnetisation as a function of the external field strength provides a second way to gain information on the crystallite size and, in the case of superparamagnetic samples, allows for the calculation of size distributions *via* application of the Langevin equation(s) [39]. Said measurements for the 1 and 3 wt.% Co/EG catalysts at 220 °C after reduction exhibit magnetic hysteresis behaviour (Figure 5), *i.e.* larger Co nanoparticles displaying remnant magnetisation upon removal of the external field were present in both catalysts. The crystallite size distribution dictates the shape of the hystereses with larger, non-superparamagnetic nanoparticles leading to a

widening due to the coercive force required to overcome the remnant magnetisation [39,54]. In addition, smaller nanoparticles result in a lower gradient, *i.e.* higher external field strengths are required in order to obtain saturation magnetisation. Hence, the 3 wt.% catalyst comprises, as expected, larger Co crystallites after reduction due to the higher loading facilitating sintering during reduction (Figure 3b). Analysis of the hysteresis of the 1 wt.% Co loaded catalyst results in a significantly lower γ value of 9.4 wt.% when compared to the catalyst with the higher loading (32.4 wt.%). It only experienced limited sintering during the reduction, which supports the hypothesised reduction behaviour as discussed with the help of the derivatives of the magnetisation during reduction (Figure 4). The DOR of the two samples is obtained *via* extrapolation of the measured magnetisations at high external field strengths (1.3, 1.7, and 2.0 T) to the inverse external field strength [39]. Both catalysts show a high reducibility with a DOR of 91.8 and 88.1% for a Co loading of 1 and 3 wt.%, respectively. It has to be noted that the 1 wt.% Co/EG catalyst was exposed to 300 °C for an extended period allowing for a higher *DOR* (Figure 3a).
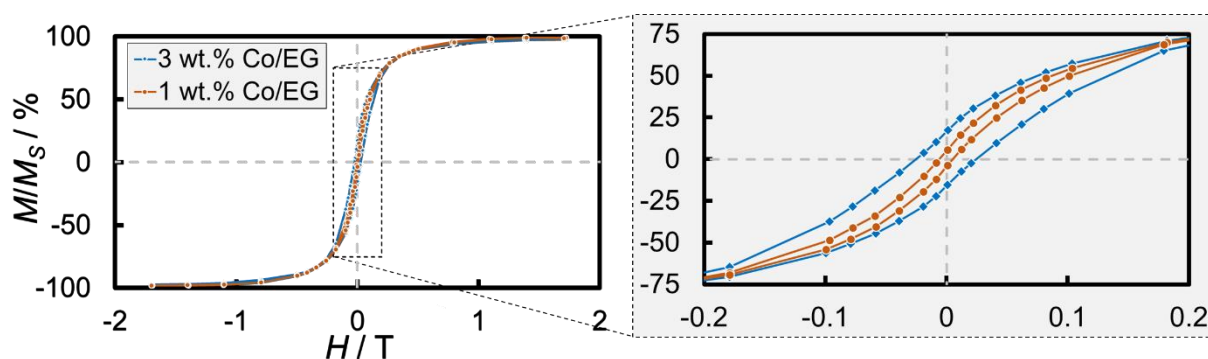

Figure 5   Sample magnetisation as a function of external field strength at 220 °C with an inset displaying the hysteresis broadening upon reduction of 3 and 1 wt.% Co on exfoliated graphite in hydrogen at 300 °C (1 °C min^{-1}) for 6 or 18 h, respectively.

The scope of the present study is the investigation of structural dependencies of catalyst deactivation mechanisms in the FTS. As the 3 wt.% Co/EG catalyst lost its well-defined structure during reduction from Co_3O_4 to metallic Co, only the catalyst with a lower loading of 1 wt.% Co was applied in the testing of the stability under FT conditions. At first, the size distribution of the smaller, superparamagnetic fraction of the Co nanoparticles (90.6 wt.% of the total Co fraction) was calculated *via* analysis of the magnetic hysteresis applying a combination of the Jiles-Atherton method [43,44] and the Langevin method [39]. As expected, the superparamagnetic nanoparticles in the reduced 1 wt.% Co/EG exhibit a narrow size distribution with a small relative volume-based standard deviation of 11% (Figure 6), which underlines the well-defined character of this model catalyst. The volume mean crystallite size of this superparamagnetic Co fraction is 5.9 nm according to the magnetic measurements. Hence, the well-defined nanoparticles retained their size and narrow size distribution after conversion into the

metallic phase. It has to be noted that different techniques for size analysis (TEM, XRD, magnetometry) are expected to have a variation in obtained sizes and hence cannot be compared directly to another. For example, distinction between reduced and non-reduced nanoparticles is challenging when analysing the passivated samples by means of TEM, while the smallest fraction (<2 nm) cannot be identified during size analysis *via* XRD.
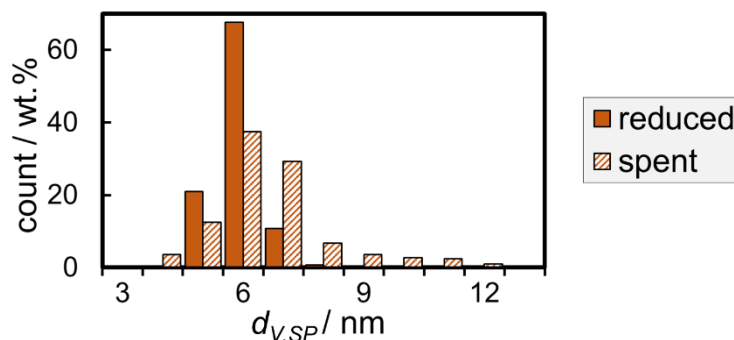

Figure 6   Crystallite size distribution of the superparamagnetic cobalt fraction in the reduced and spent 1 wt.% Co on exfoliated graphite model catalyst as obtained *via* a combined application of the Jiles-Atherton and the Langevin method on the measurement of the magnetisation as a function of the external field strength.

After reduction of the 1 wt.% Co/EG model catalyst, the sample was exposed to dry FT conditions with a synthesis gas partial pressure of 2.14 bar in 0.46 bar inert gas (Table 1). The high GHSV of 17537 mL ($g_{catalyst}$ h)$^{-1}$ ensured a low CO conversion of 0.1% resulting in a low partial pressure of the FT product H_2O. Hence, the probability of potential H_2O-induced morphological changes, such as oxidation of Co to CoO, is limited. However, the magnetisation of the catalyst decreases sharply upon introduction of synthesis gas indicating a phase transformation of metallic, ferromagnetic Co (Figure 7a). In fact, adsorption of CO and the formation of hydrocarbon chains on the Co surface may decrease the magnetisation of surface Co atoms as well [10,12,13], but the loss in magnetisation of over 20% cannot be solely explained by such adsorption processes. The dispersion of Co for the obtained size distribution of the reduced catalyst is ~17%, *i.e.* not even full cancelation of the magnetisation of Co surface atoms due to adsorption can fully account for the observed loss in magnetisation. Hence, the amount of metallic Co must have decreased due to oxidation and/or carburisation. The γ value increases from 9.4 to 11-12 wt.% within 30 min TOS, while the remnant magnetisation remains constant within this time range (Figure 7b-c). Such a preferential loss in smaller Co crystallites may indicate partial oxidation of the smallest crystallites [11,12,48]. Nevertheless, adsorption effects [10] become significantly stronger for small crystallite sizes and contribute to these observations as well. After 5 h under dry synthesis gas, the loss in magnetisation is less pronounced (Figure 7a). Carburisation of Co may account for the loss in magnetisation

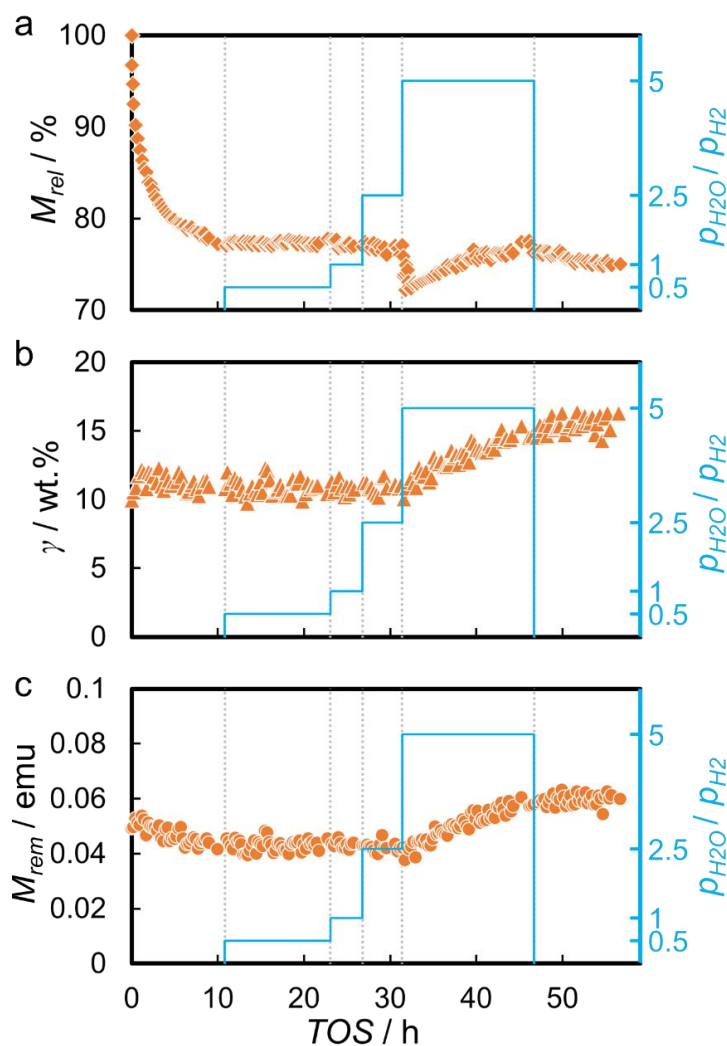together with adsorbed hydrocarbon species decreasing the surface magnetisation [10,55].

Figure 7 (a) Magnetisation at maximal field strength (2 T) relative to the magnetisation after reduction, (b) fraction of ferromagnetic cobalt displaying remnant magnetisation upon removal of the external field, and (c) remnant magnetisation of the 1 wt.% Co on exfoliated graphite model catalyst at 220 °C as a function of time on stream at stepwise increasing ratios of the partial pressures of water to hydrogen (solid).

Surprisingly, the introduction of co-fed H_2O (p_{H2O}/p_{H2} = 0.5) stabilises the magnetisation of the catalyst (Figure 7a). H_2O-originated species show a high stability on the Co surface [12,13,56–58] and may stabilise the metallic phase by decreasing the rate of carburisation. The magnetisation of the model catalyst does not change significantly when exposed to an increased p_{H2O}/p_{H2} ratio of 1. Hence, oxidation or a dominant adsorption of OH* over CO* species [12,13] are not at play as the partial pressure of CO (0.69 bar) is sufficiently high [13]. Exposure of the catalyst to a p_{H2O}/p_{H2} ratio of 2.5 may have induced oxidation to a small extent, but the potentially identified decrease in magnetisation lies within the error of measurement (Figure 7a). This

relatively high stability of the Co nanoparticles experiencing little stabilisation by the graphitic support material may be explained by the absence of small nanoparticles (<4 nm), which are typically present in impregnated Co-based FT catalysts [6,59,60] and are expected to display little resistance against oxidation [6,11,12,48].

The magnetisation of the catalyst decreases rapidly at a p_{H2O}/p_{H2} ratio of 5, but unexpectedly recovers slowly after 1 h TOS at a constant p_{H2O}/p_{H2} ratio (Figure 7a). Hence, metallic Co is initially oxidised to anti-ferromagnetic cobalt oxide when exposed to this increased level of H_2O, but subsequently re-reduces at prolonged exposure time. At first glance, this observation seems to be contradictory, but an increase in the γ value (Figure 7b), respectively the fraction of ferromagnetic Co displaying remnant magnetisation (Figure 7c), may provide an explanation for this phenomenon. Said continuous increase is originated in a formation of metallic Co of an increased crystallite size, while the initial decrease in magnetisation is correlated to H_2O-induced oxidation of the nanoparticles with oxygen derived from CO dissociation [13]. The latter process is hypothesised to induce a high mobility of the (partially) oxidised intermediate crystallites due to adsorbed O* species initiating crystallite migration, collision, and eventually crystallite coalescence [8]. The oxidised, anti-ferromagnetic crystallites of increased size are then re-reduced due to a previously identified size-dependent phase transition between Co and CoO in H_2O/H_2 atmospheres [11,12,48] (Figure S9), $i.e.$ the metallic Co phase represents the stable phase for the new increased crystallite size under given conditions when compared to CoO. These observations are, to our knowledge, a first time experimental proof for an interconnection between H_2O-induced oxidation and hydrothermal sintering of Co nanoparticles. Furthermore, the observed re-reduction upon sintering evidences, once again, the size-dependent stability of Co under H_2O-rich conditions [11,12,48]. The magnetisation and the γ value continuously increase during exposure to a p_{H2O}/p_{H2} ratio of 5 until the initial level of the magnetisation before co-feeding H_2O is obtained after 43 h TOS (Figure 7a-b). This full reversibility strongly suggests the exclusive participation of previously reduced Co crystallites in the identified oxidation and sintering process, $i.e.$ cobalt oxide species present after initial reduction of the catalyst remain spectator species during the exposure to H_2O and said deactivation process. This further suggests that sintering takes place in an oxidised phase, which is not ferromagnetic but also not fully oxidised. Such an intermediate phase has been proposed in literature [8] and consequently represents the phase with a drastically increased mobility.

Removing H_2O from the feed stream generally allows for a reversibility of thermodynamically controlled processes. As the magnetisation does not increase upon removal of H_2O from the feed stream in the present study (Figure 7a), the observed re-reduction at a p_{H2O}/p_{H2} ratio of 5 is indeed exclusively associated to the Co nanoparticles which were oxidised upon exposure to H_2O. In contrast, exposure to dry synthesis gas slowly decreases the magnetisation of the model catalyst indicating carburisation of the

catalyst as observed during the initial 10 h TOS. The decrease of the magnetisation follows a trend comparable to the behaviour before co-feeding H_2O (Figure 7a).

Measuring the magnetisation as a function of the external field strength with a combined application of the Jiles-Atherton method [43,44] and the Langevin equation [39] enables the analysis of the crystallite size and distribution of the superparamagnetic Co fraction [13], *i.e.* the smaller Co crystallites. Comparison of this experimental analysis of the evolution of the crystallite sizes with thermodynamic predictions by van Steen *et al.* [48] visualises the interconnectivity between oxidation to CoO and hydrothermal sintering (Figure 8). The presence of the fcc-Co allotrope has previously been identified after reduction of the model catalyst in H_2 [20] and hence the thermodynamic predictions are based on this allotrope. Neither the mean size of 5.9 nm, nor the narrow size distribution of the Co phase after reduction is affected by the exposure to p_{H2O}/p_{H2} ratios of 0.5-2.5, which strongly supports the absence of morphological changes. When the ratio is increased to 5, the smaller crystallites below the critical size for oxidation at given conditions (5.4 nm according to thermodynamic predictions [48]) become unstable as the oxidic phase is thermodynamically favoured (Figure 8). In turn, these small crystallites oxidise, which agrees well with the thermodynamic prediction for the stability region of metallic Co. The formed Co oxide precursors are postulated to exhibit an increased mobility resulting in sintering [8]. The volume mean size of the superparamagnetic fraction shifts from 5.9 to 6.7 nm, while the non-superparamagnetic fraction increases from 10 to 15 wt.% (Figure 7b). In consequence, this size increase results in a re-reduction to metallic Co crystallites. Accordingly, the obtained relative volume-based standard deviation of the superparamagnetic fraction increases from 11 to 41% (Figure 8). The final size distribution, as obtained from the magnetic hysteresis, exhibit significant amounts of crystallites up to 10 nm (Figure 6) and is identical to the one after exposure of the catalyst to a p_{H2O}/p_{H2} of 5. This observation once again demonstrates the absence of major morphological changes when removing H_2O from the feed stream. When compared to the previous hystereses, the widening of the hysteresis loop is more pronounced in these last two hystereses (Figure S10) visualising the increase in crystallite size.
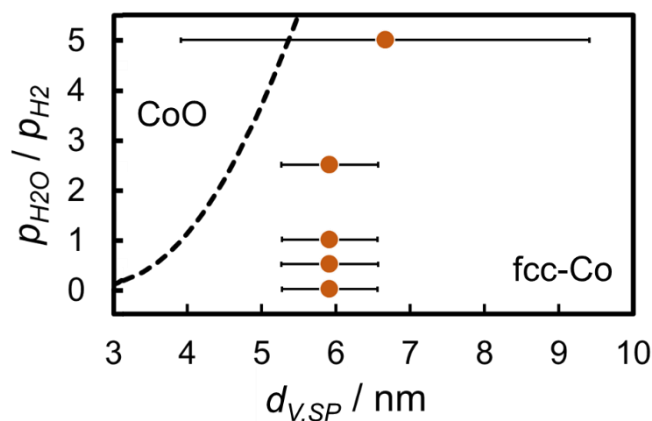
Figure 8 Comparison of the volume-mean crystallites sizes with standard deviation of cobalt crystallites as obtained from a combined application of the Jiles-Atherton method and the Langevin method on the measurement of the magnetisation as a function of the external field strength after exposure of 1 wt.% Co on exfoliated graphite to various water-rich environments. The data is superimposed on the size-dependent thermodynamic equilibrium of the oxidation of fcc-cobalt crystallites in the nanometre size regime to cobalt(II) oxide [48] (dashed) as calculated for 220 °C.

Monitoring the CO conversion and selectivity of the 1 wt.% Co/EG model catalyst during the experiment in the magnetometer provides further insight into the availability of FT active species, *i.e.* metallic Co surface atoms. It has to be noted that the low CO conversion of 0.1% results in rather large errors during analysis of activity and selectivity. Nevertheless, co-feeding of H_2O seemingly increases the CO conversion upon exposure to a p_{H2O}/p_{H2} ratio of 0.5 (Figure 9), which is in line with a reported beneficial effect of H_2O on the reaction rate at moderate concentration levels of H_2O [30,61–67]. Contrarily, the exposure of the catalyst to p_{H2O}/p_{H2} ratios of 1 and 2 lowers the CO conversion to the initial level. Observed effects of H_2O on the product distribution can be summarised by increased selectivity of hydrocarbon chains and suppressed secondary reactions of olefins (Figure S11), which confirms reported trends for the partial pressure of H_2O in literature [5,30,62,63,66,68,69]. The proposed role of H_2O includes an enhancement of the CO dissociation [62,70,71] and an inhibition of secondary reactions [69] at increased partial pressures. The size increase due to the observed oxidation and hydrothermal sintering process at a p_{H2O}/p_{H2} ratios of 5 result in an expected significant drop of the catalyst's activity (Figure 9), *i.e.* deactivation due to the loss of surface area. The CO conversion after removing H_2O from the feed stream is comparable. In fact, the decrease in Co dispersion according to obtained volume mean crystallite sizes from magnetic measurements is approximately 50%, which corresponds well to the observed irreversible deactivation of 30-55% of the initial conversion upon exposure to a p_{H2O}/p_{H2} ratio of 5 (Figure 9).
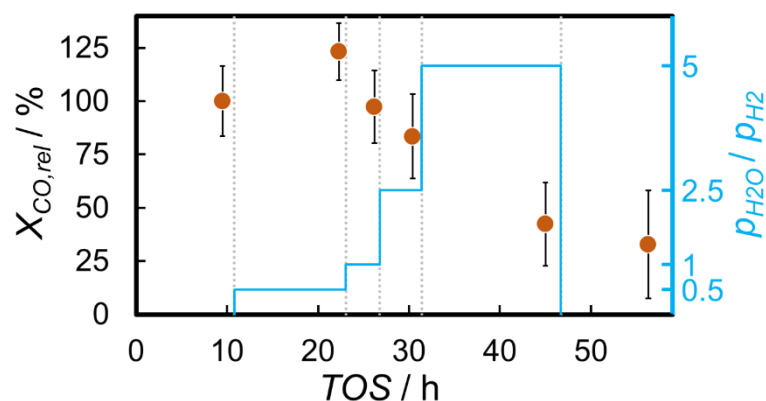
17

Figure 9   Conversion of carbon monoxide over 1 wt.% Co on exfoliated graphite relative to the initial conversion as a function of time on stream at stepwise increasing ratios of the partial pressures of water to hydrogen (solid) at 220 °C.

TEM analysis of the spent and passivated catalyst also confirms an increase in the volume-mean crystallite size to 10.0 nm with a relative standard deviation of 35% (Figure 10). This is significant larger than the volume-mean size obtained from magnetic measurements of the superparamagnetic Co fraction, but also comprises the approximately 15 wt.% of Co nanoparticles that are larger than the critical size for superparamagnetism. The obtained number-based size distribution is tailing to larger crystallite sizes indicating sintering of nanoparticles with an initial size of 4-6 nm to sizes up to 17 nm. Comparison of the size distribution in the spent catalyst as obtained by means of TEM analysis with thermodynamic predictions on the stability of Co in H_2O-rich environment [48] (Figure 8) results in a reasonable match (Figure S12) confirming the herein concluded results.
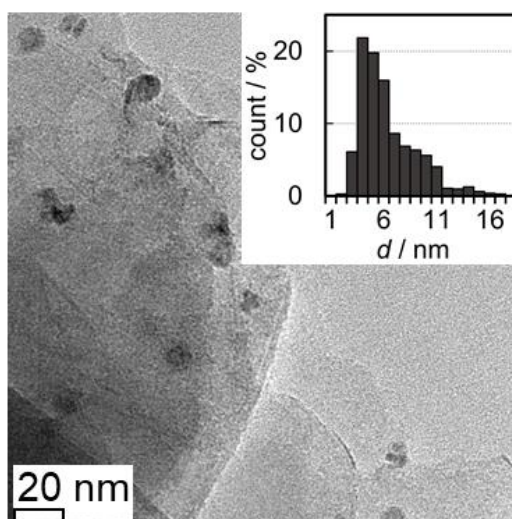

Figure 10   Transmission electron micrograph of the spent and passivated 1 wt.% Co on exfoliated graphite model catalyst with number-based size distribution of the nanoparticles.

Similar experiments were previously conducted using common metal oxide supports and increased Co loadings [10–12]. Here, significant sintering was only at play when exposing a Co/Al_2O_3 catalyst to combined high partial pressures of CO and H_2O [10]. In contrast, oxidation and/or the formation of a metal-support compound was observed in all studies. In addition, the phase transformation of metallic Co *via* said formation of metal-support compounds was recently isolated applying similar model catalysts with various metal oxides as support materials in a comparative study [72]. The extent of this H_2O induced phase transformation was shown to be strongly dependent on the support material, which in turn prohibits general conclusions on the contribution/feasibility of the various potential deactivation pathways.

4. Summary and conclusions

A newly developed model catalyst system, cobalt on exfoliated graphite, was exposed to synthesis gas with a sufficiently high partial pressure of carbon monoxide enabling indirect, intrinsic oxidation of cobalt to cobalt(II) oxide. The utilisation of a carbonaceous support allows for the isolation of said oxidation process preventing an underlying formation of cobalt-support compounds. A rapid oxidation of the cobalt phase was observed under simulated high FT conversion levels confirming reported thermodynamic predictions. Surprisingly, the oxidised cobalt re-reduced most likely due to an increase in the crystallite size *via* hydrothermal sintering in a (partially) oxidised phase, which is associated to the oxidation process in accordance with a hypothesised mechanism in literature. The re-reduction further exhibits the size-dependent stability of cobalt nanoparticles against oxidation to cobalt(II) oxide. Capturing this interconnection between water-induced oxidation and sintering with subsequent re-reduction of the sintered crystallites *in situ* represents a first in research on deactivation of cobalt-based FT catalysts.

References

[1] E. Iglesia, Appl. Catal. A Gen. 161 (1997) 59–78.
[2] J. van de Loosdrecht, B. Balzhinimaev, J.-A. Dalmon, J.W. Niemantsverdriet, S. V. Tsybulya, A.M. Saib, P.J. van Berge, J.L. Visagie, Catal. Today. 123 (2007) 293–302.

[3]   A.K. Dalai, B.H. Davis, Appl. Catal. A Gen. 348 (2008) 1–15.

[4]   N.E. Tsakoumis, M. Rønning, Ø. Borg, E. Rytter, A. Holmen, Catal. Today. 154 (2010) 162–182.

[5]   E. Rytter, A. Holmen, ACS Catal. 7 (2017) 5321–5328.

[6]   N.E. Tsakoumis, J.C. Walmsley, M. Rønning, W. van Beek, E. Rytter, A. Holmen, J. Am. Chem. Soc. 139 (2017) 3706–3715.

[7]   G.L. Bezemer, T.J. Remans, A.P. van Bavel, A.I. Dugulan, J. Am. Chem. Soc. 132 (2010) 8540–8541.

[8]   M. Sadeqzadeh, J. Hong, P. Fongarland, D. Curulla-Ferré, F. Luck, J. Bousquet, D. Schweich, A.Y. Khodakov, Ind. Eng. Chem. Res. 51 (2012) 11955–11964.

[9]   E. Rytter, A. Holmen, Catalysts. 5 (2015) 478–499.

[10] M. Claeys, M.E. Dry, E. van Steen, P.J. van Berge, S. Booyens, R. Crous, P. van Helden, J. Labuschagne, D.J. Moodley, A.M. Saib, ACS Catal. 5 (2015) 841–852.

[11] N. Fischer, B. Clapham, T. Feltes, E. van Steen, M. Claeys, Angew. Chemie Int. Ed. 53 (2014) 1342–1345.

[12] M. Wolf, H. Kotzé, N. Fischer, M. Claeys, Faraday Discuss. 197 (2017) 243–268.

[13] M. Wolf, B.K. Mutuma, N.J. Coville, N. Fischer, M. Claeys, ACS Catal. 8 (2018) 3985–3989.

[14] A. Tavasoli, R.M. Malek Abbaslou, A.K. Dalai, Appl. Catal. A Gen. 346 (2008) 58–64.

[15] M.E. Dry, FT Catalysts, in: A.P. Steynberg, M.E. Dry (Eds.), Fischer-Tropsch Technol., Elsevier, Amsterdam, 2004: pp. 533–600.

[16] G. Kiss, C.E. Kliewer, G.J. DeMartin, C.C. Culross, J.E. Baumgartner, J. Catal. 217 (2003) 127–140.

[17] H. Karaca, J. Hong, P. Fongarland, P. Roussel, A. Griboval-Constant, M. Lacroix, K. Hortmann, O. V. Safonova, A.Y. Khodakov, Chem. Commun. 46 (2010) 788–790.

[18] M. Sadeqzadeh, S. Chambrey, S. Piché, P. Fongarland, F. Luck, D. Curulla-Ferré, D. Schweich, J. Bousquet, A.Y. Khodakov, Catal. Today. 215 (2013) 52–59.

[19] M. Sadeqzadeh, S. Chambrey, J. Hong, P. Fongarland, F. Luck, D. Curulla-Ferré, D. Schweich, J. Bousquet, A.Y. Khodakov, Ind. Eng. Chem. Res. 53 (2014) 6913–6922.

[20] M. Wolf, N. Fischer, M. Claeys, ChemRxiv, Employing exfoliated graphite as novel support material for heterogeneous model catalysts, 2019, Preprint, DOI: 10.26434/chemrxiv.8079620.

[21] M. Claeys, E. van Steen, J.L. Visagie, J. van de Loosdrecht, Magnetometer, US Patent 8,773,118 B2, 2014.

[22] S.J. Tauster, S.C. Fung, R.T.K. Baker, J.A. Horsley, Science (80-.). 21 (1981) 1121–1125.

[23] S.J. Tauster, Acc. Chem. Res. 20 (1987) 389–394.

[24] M. Wolf, E.K. Gibson, E.J. Olivier, J.H. Neethling, C.R.A. Catlow, N. Fischer, M. Claeys, Catal. Today. In Press (2019).

[25] N. Shi, W. Cheng, H. Zhou, T. Fan, M. Niederberger, Chem. Commun. 51 (2015) 1338–1340.

[26] M. Wolf, N. Fischer, M. Claeys, Mater. Chem. Phys. 213 (2018) 305–312.

[27] Y. Hernandez, V. Nicolosi, M. Lotya, F.M. Blighe, Z. Sun, S. De, I.T. McGovern, B. Holland, M. Byrne, Y.K. Gun'Ko, J.J. Boland, P. Niraj, G. Duesberg, S. Krishnamurthy, R. Goodhue, J. Hutchison, V. Scardaci, A.C. Ferrari, J.N. Coleman, Nat. Nanotechnol. 3 (2008) 563–568.

[28] U. Khan, A. O'Neill, M. Lotya, S. De, J.N. Coleman, Small. 6 (2010) 864–871.

[29] N. Fischer, E. van Steen, M. Claeys, Catal. Today. 171 (2011) 174–179.

[30] N. Fischer, B. Clapham, T. Feltes, M. Claeys, ACS Catal. 5 (2015) 113–121.

[31] T.W. van Deelen, J.J. Nijhuis, N.A. Krans, J. Zečević, K.P. de Jong, ACS Catal. 8 (2018) 10581–10589.

[32] ICDD, PDF-2 Release 2008 (Database), International Centre for Diffraction Data, Newtown Square, USA, 2008.

[33] H.M. Rietveld, J. Appl. Crystallogr. 2 (1969) 65–71.

[34] A.A. Coelho, J. Appl. Crystallogr. 36 (2003) 86–95.

[35] P. Scherrer, Nachrichten von Der Gesellschaft Der Wissenschaften Zu Göttingen, Math. Klasse. (1918) 98–100.

[36] G. Bergeret, P. Gallezot, Particle Size and Dispersion Measurements, in: G. Ertl, H. Knözinger, F. Schüth, J. Weitkamp (Eds.), Handb. Heterog. Catal., 2nd ed., Wiley-VCH, Weinheim, Germany, 2008: pp. 738–765.

[37] W. Rasband, ImageJ 1.51a, National Institute of Mental Health, Bethesda, USA, 2016.

[38] E.P. Barrett, L.G. Joyner, P.P. Halenda, J. Am. Chem. Soc. 73 (1951) 373–380.

[39] J.-A. Dalmon, Magnetic measurements and catalysis, in: B. Imelik, J.C. Vedrine (Eds.), Catal. Charact. Phys. Tech. Solid Mater., Plenum Press, New York, 1994: pp. 585–609.

[40] K.J. Carroll, Z.J. Huba, S.R. Spurgeon, M. Qian, S.N. Khanna, D.M. Hudgins, M.L. Taheri, E.E. Carpenter, Appl. Phys. Lett. 101 (2012) 012409.

[41] A. Barbier, A. Hanif, J.-A. Dalmon, G.A. Martin, Appl. Catal. A Gen. 168 (1998) 333–343.

[42] K. Holt, L. Jewell, H. Niemantsverdriet, L. Macheli, M. Shozi, G. Hutchings, T. Wezendonk, M. Bowker, R. Catlow, S. Adam, P.J. Kooyman, E. Hensen, J. Hayward, N. Coville, K.-J. Weststrate, N. Fischer, A. Roldan, E. Redekop, E. van Steen, H. Friedrich, D.-H. Kuo, H. Bandaru, L. Deeplal, A. Zivkovic, K. Naiker, C. Tucker, T.P.O. Mkhwanazi, D. Bahnemann, M. Neurock, A. Petersen, R.P. Forbes, T. Phaahlamohlaka, H. Schulz, D. Lennon, U. Olsbye, M. Wolf, S. Kondrat, P. Collier, X. Sun, Y. Zheng, A. Corma, E. Iglesia, T. Nyathi, D. Ma, M. Bremmer, M. Claeys, F. Kapteijn, Faraday Discuss. 197 (2017) 353–388.

[43] D.C. Jiles, D.L. Atherton, J. Appl. Phys. 55 (1984) 2115–2120.

[44] D.C. Jiles, D.L. Atherton, J. Magn. Magn. Mater. 61 (1986) 48–60.

[45] N.C. Pop, O.F. Caltun, J. Optoelectron. Adv. Mater. 12 (2010) 885–891.

[46] E. Sárospataki, M. Kuczmann, J. Electr. Eng. 57 (2006) 40–43.

[47] J. Paterson, M. Peacock, E. Ferguson, M. Ojeda, J. Clarkson, Appl. Catal. A Gen. 546 (2017) 103–110.

[48] E. van Steen, M. Claeys, M.E. Dry, J. van de Loosdrecht, E.L. Viljoen, J.L. Visagie, J. Phys. Chem. B. 109 (2005) 3575–3577.

[49] M. Wolf, N. Fischer, M. Claeys, Catal. Today. 275 (2016) 135–140.

[50] H. Schulz, W. Boehringer, C. Kohl, N. Rahman, A. Will, Entwicklung und Anwendung der Kapillar-GC Gesamtproben-Technik für Gas/Dampf Vielstoffgemische, in: DGMK Forschungsbericht 320, DGMK, Hamburg, 1984: pp. 320–329.

[51] H. Knözinger, Temperature-Programmed Reduction and Oxidation, in: G. Ertl, H. Knözinger, F. Schüth, J. Weitkamp (Eds.), Handb. Heterog. Catal., 2nd ed., Wiley-VCH, Weinheim, Germany, 2008: pp. 1080–1096.

[52] S.P.S. Andrew, Chem. Eng. Sci. 36 (1981) 1431–1445.

[53] O. Levenspiel, Chemical Reaction Engineering, 3rd ed., Wiley, New York, 1999.

[54] P.A. Chernavskii, J.-A. Dalmon, N.S. Perov, A.Y. Khodakov, Oil Gas Sci. Technol. 64 (2009) 25–48.

[55] M. Claeys, M.E. Dry, E. van Steen, E. du Plessis, P.J. van Berge, A.M. Saib, D.J. Moodley, J. Catal. 318 (2014) 193–202.

[56] I.A.W. Filot, R.A. van Santen, E.J.M. Hensen, Angew. Chemie Int. Ed. 53 (2014) 12746–12750.

[57] A.C. Kizilkaya, J.W. Niemantsverdriet, C.J. Weststrate, J. Phys. Chem. C. 120 (2016) 4833–4842.

[58] P. van Helden, J.-A. van den Berg, M.A. Petersen, W.J. van Rensburg, I.M. Ciobîcă, J. van de Loosdrecht, Faraday Discuss. 197 (2017) 117–151.

[59] D.J. Moodley, A.M. Saib, J. van de Loosdrecht, C.A. Welker-Nieuwoudt, B.H. Sigwebela, J.W. Niemantsverdriet, Catal. Today. 171 (2011) 192–200.

[60] T. Jermwongratanachai, G. Jacobs, W.D. Shafer, W. Ma, V.R.R. Pendyala, B.H. Davis, B. Kitiyanan, S. Khalid, D.C. Cronauer, A.J. Kropf, C.L. Marshall, Top. Catal. 57 (2014) 479–490.

[61] A.M. Hilmen, D. Schanke, K.F. Hanssen, A. Holmen, Appl. Catal. A Gen. 186 (1999) 169–188.

[62] C.J. Bertole, C.A. Mims, G. Kiss, J. Catal. 210 (2002) 84–96.

[63] S. Krishnamoorthy, M. Tu, M.P. Ojeda, D. Pinna, E. Iglesia, J. Catal. 211 (2002) 422–433.

[64] M. Lualdi, S. Lögdberg, M. Boutonnet, S. Järås, Catal. Today. 214 (2013) 25–29.

[65] S. Lögdberg, M. Boutonnet, J.C. Walmsley, S. Järås, A. Holmen, E.A. Blekkan, Appl. Catal. A Gen. 393 (2011) 109–121.

[66] J. Li, G. Jacobs, T. Das, Y. Zhang, B. Davis, Appl. Catal. A Gen. 236 (2002) 67–76.

[67] T.K. Das, W.A. Conner, J. Li, G. Jacobs, M.E. Dry, B.H. Davis, Energy & Fuels. 19 (2005) 1430–1439.

[68] S. Storsæter, Ø. Borg, E.A. Blekkan, A. Holmen, J. Catal. 231 (2005) 405–419.

[69] H. Schulz, M. Claeys, S. Harms, Stud. Surf. Sci. Catal. 107 (1997) 193–200.

[70] M. Claeys, E. van Steen, Catal. Today. 71 (2002) 419–427.

[71] A.M. Saib, D.J. Moodley, I.M. Ciobîcă, M.M. Hauman, B.H. Sigwebela, C.J. Weststrate, J.W. Niemantsverdriet, J. van de Loosdrecht, Catal. Today. 154 (2010) 271–282.

[72] M. Wolf, E.K. Gibson, E.J. Olivier, J.H. Neethling, C.R.A. Catlow, N. Fischer, M. Claeys, ACS Catal. 9 (2019) 4902–4918.